GEOPHYSICAL RESEARCH LETTERS, VOL. 28, NO. 12, PAGES 2321-2324, JUNE 15, 2001

Geodetic detection of active faults in S. California

Shimon Wdowinski and Yonadav Sudman

Department of Geophysics and Planetary Sciences, Tel Aviv University Ramat Aviv, Israel

Yehuda Bock

IGPP, Scripps Institution of Oceanography, La Jolla, California

Abstract. A new analysis of velocities of geodetic markers straddling the San Andreas Fault System in southern California reveals that interseismic deformation is localized along a dozen sub-parallel narrow belts of high shear strain rate that correlate well with active geologic fault segments and locally with concentrated zones of microseismicity. High shear strain rates (0.3-0.95 μstrain/year) are observed northward and southward of the San Andreas fault's big bend, whereas the big bend itself is characterized by a diffuse low magnitude shear strain rate. Dilatational deformation is diffuse and of relatively low magnitude (< 0.2 μstrain/year), with the highest contraction rates occurring in the Ventura and Los Angeles basins. Because no prior assumptions were made regarding the geology, tectonics, or seismicity of the region, our analysis demonstrates that geodetic observations alone can be used to detect active fault segments.

Introduction

Prior knowledge of the location of active faults can help in earthquake mitigation. Over the past 25 years, however, the largest magnitude and most destructive earthquakes in southern California (1971 San Fernando, 1992 Landers, 1994 Northridge, and 1999 Hector Mine earthquakes) occurred along faults that were not detected either seismically or geologically prior to these events. Here we investigate the use of geodetic observations to detect active faults in southern California. We apply a new quasi two-dimensional analysis method, based on the Pole of Rotation reference frame [*Wdowinski*, 1998], that allows us to map narrow belts of high strain rate from the Southern California Earthquake Center (SCEC) velocity field version 2.0. Previous two-dimensional deformation analyses of these data detected the overall strain rate concentration along the entire length of San Andreas Fault System (SAFS) [*Jackson et al.*, 1997; *Shen-Tu et al.*, 1999]. Our analysis, however, has higher spatial resolution and enables us to detect a dozen sub-parallel narrow belts of high strain rate. The location of the belts correlate well with active geologic fault segments and locally with concentrated zones of microseismicity.

The SCEC velocity field

The SCEC velocity field version 2.0 is a systematic analysis of terrestrial and space geodetic data acquired in southern California over the past 25 years, representing the interseismic velocity field with respect to stable North America. It was compiled by the SCEC's Crustal Deformation Working Group and is accessible at the SCEC Web site (http://www.scecdc.scec.org/group_e/release.v2). The data set contains 363 velocity vectors, from which we use the 349 vectors free of postseismic deformation, covering an area of roughly 30,000 km^2. Unlike *Shen-Tu et al.* [1999], who combined several disjoint geodetic data sets to obtain larger spatial coverage, we use only the SCEC velocities, which were calculated in a single consistent reference frame.

The SCEC velocity vectors are oriented to the northwest along the expected direction of Pacific plate motion with respect to North America. However, a comparison between the observed velocities and the directions predicted by the NUVEL-1A global plate motion model shows a 2-3° misalignment as pointed out previously by *Shen-Tu et al.* [1999]. This misalignment indicates that the NUVEL-1A pole of rotation (PoR) reference frame is inappropriate for deformation analysis of the SCEC velocity data. Its use would introduce an additional rotational component to the velocity field which would be interpreted erroneously as deformation. We define a new pole of deformation (PoD) reference frame for the SCEC velocity field using the following minimization criterion:

$$\chi^2 = \Sigma(V_\theta/\sigma_{V\theta})^2 = min, \qquad (1)$$

where V_θ is the latitudinal velocity component and $\sigma_{V\theta}$ is its standard deviation, expressed in the new reference frame. This frame, which is fixed to stable North America, minimizes the misalignment between the observed velocities and the directions of small circles about the new pole. The PoD was found by a systematic search along a dense grid of points that cover a large area (20°x20°) around the NUVEL-1A pole (48.7°N, 281.8°E). Our calculations reveal that the PoD is located at (52.0°N, 287.0°E), which lies significantly away from the NUVEL-1A PoR, but very close to a recent calculation of the Pacific-North America PoR (51.5°N, 286.3°E) from GPS data [*DeMets and Dixon*, 1999]. Elimination of diverging velocity vectors may shift somewhat the PoD location but not significantly, because most of the SCEC velocities are parallel to one another. Using the average velocity of the 15 westernmost sites, which represent or almost represent the Pacific plate motion, we calculated an angular velocity of 0.62°/Ma that is used to normalize the velocity vectors in the PoD reference frame.

Figure 1 shows the transformed normalized velocity field superimposed on the main geologic fault segments in southern California. We present these data in a planar Cartesian projection, in order to emphasize the alignment between the velocity vectors and the vertical ("latitudinal") grid lines, which are projections of small circles about the PoD. Figure 1 also shows very good agreement between the direction of

Paper number 2000GL012637.
0094-8276/01/2000GL012637$05.00

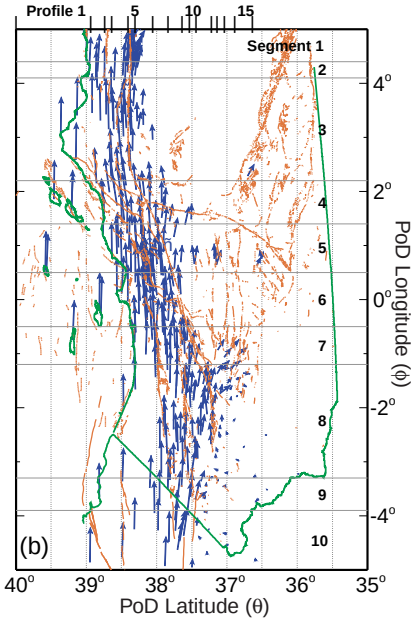

Figure 1. The SCEC velocity field version 2.0 for southern California in the PoD reference frame. Horizontal dotted lines represent the boundaries between the 10 segments of similar velocity transition. The vertical lines are grid lines representing small circles about the PoD. The number along the upper frame represents the location of 15 longitudinal profiles of similar velocity transition.

most major fault segments and the vertical grid lines, suggesting that the PoD reference frame is also the preferred one for representing the long-term (geological) deformation.

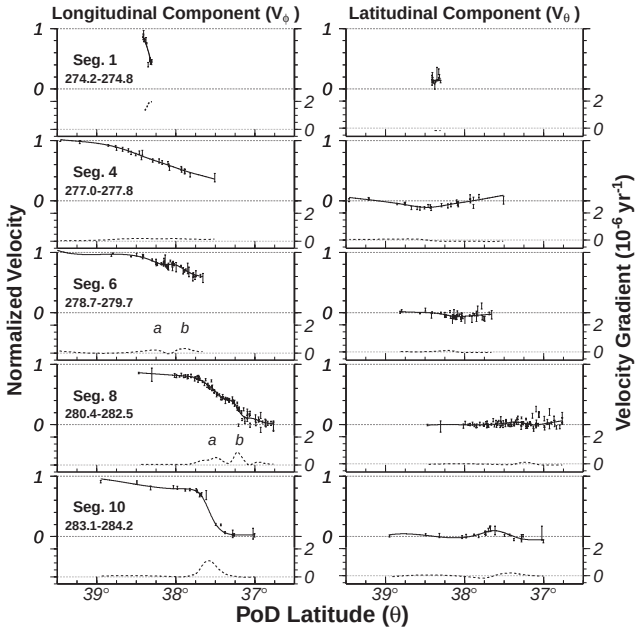

Figure 2. Observed and modeled (solid lines) normalized velocities across 5 of the 10 segments of similar velocity transition. The velocities are normalized by 0.62°/Ma (46-48 mm/yr depending on the distance from the PoD). Velocity gradients are shown by dashed lines on the bottom portion of each graph. The letters a and b in segments 6 and 8 mark two localized strain rate peaks.

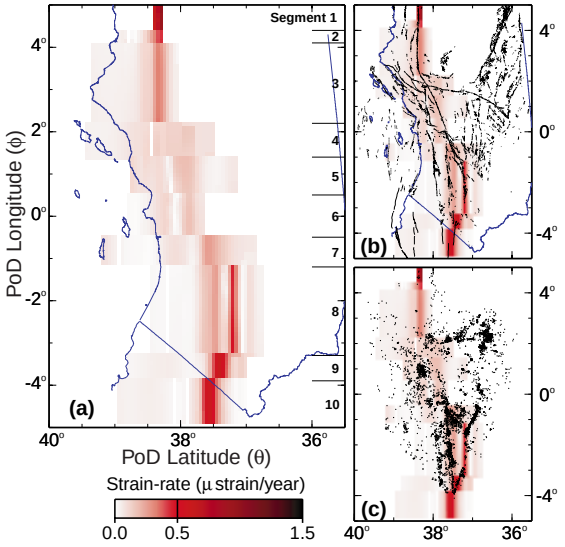

Figure 3. Maps showing the (a) distribution and magnitude of the shear strain rate, (b) the relation to the geographic location of major fault segments, and (c) the relation to concentrations of seismic activity, as recorded in 1997 (see text).

The misfit between the NUVEL-1A predicted motion direction and the orientation of major fault segments in southern California was noted previously by *Humphreys and Weldon* [1994], who analyzed the integrated motion across quaternary faults.

Velocity and strain rate analyses

Using the PoD reference frame allows us to approximate the velocity transition between the Pacific and North American plates by a single quantity: the magnitude of the longitudinal velocity component (V_ϕ). Spatial analysis of this component reveals that the velocity transition between the two plates can be characterized by 10 segments (Figure 1). The segments were determined empirically by selecting the

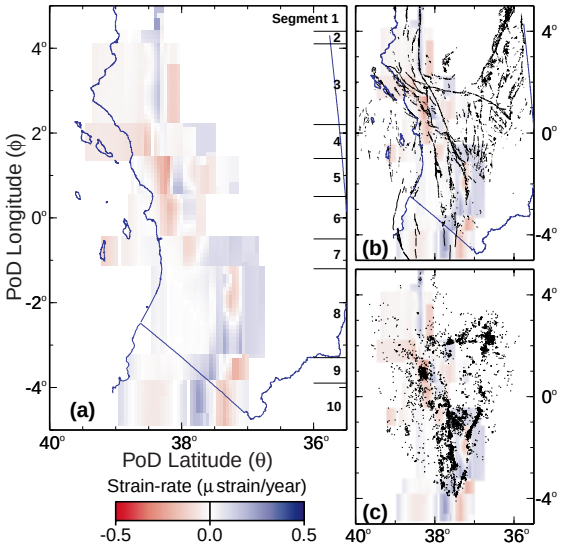

Figure 4. Same as Figure 3 except for dilatation rate. Negative values (red) represent contraction, whereas positive values (blue) represent extension.

Table 1. List of the geodetically observed velocity transition segments and their derived deformation parameters compared with geologic and seismic observations.

Geodesy						Geology		Seismicity	
Segment number	Length, km	V_{SEG}, mm/yr		γ_{MAX}, μstrain/yr	V_{LOC}, mm/yr	Fault segment	V_{GEOL}, mm/yr	Number of events	Depth, km
1	40	20		0.95	20	SAF- Parkfield	34±5	8	11.4±6.7
2	20	25		0.47	22	SAF- Cholame	34±5	1	12.5
3	130	30		0.34	20	SAF- Carrizo	34±3	52	10.8±5.8
4	55	30		0.09		SAF- Mojave	30±8		
5	60	29		0.16	15	SAF- Mojave	30±8	93	6.4±3.6
6	60	22	a	0.11	8	Newport- Inglewood	0.5±0.5	182	4.9±4.0
			b	0.16	10	SAF-Mojave	30±8	219	6.0±3.9
7	50	41	a	0.10	10	EF-Glen Ivy	5±2	92	3.0±4.0
			b	0.25	18	SAF-San Bernadino	24±5	953	9.1±6.5
8	145	40	a	0.27	17	San Jacinto Fault	12±6	1225	8.8±5.6
			b	0.45	12	SAF-Coachella	25±5	842	3.8±3.3
9	40	40		0.53	31	Imperial	30±5	219	7.5±4.5
10	90	42		0.58	33	Cerro Prieto	40-45		

V_{SEG}, V_{LOC} and V_{GEOL} denote the observed velocity across the entire segment, modeled velocity across a localized shear belt, and geologically estimated slip rate, respectively. γ_{MAX} is the maximum observed shear strain rate within each shear belt. Subsegments, marked by letters, correspond to left-to-right parallel shear belts within a single segment (Figures 2 and 3). Most geological fault segments and slip rates were obtained from *Working Group on California Earthquake Probabilities* [1995]; EF corresponds to Elsinore fault. The slip rate for the Newport-Inglewood, and Cerro Prieto segments are obtained from *Grant et al.* [1997] and *Bennett et al.* [1996], respectively. Microseismicity depth values are obtained from *Richards-Dinger and Shearer* [2000].

maximum longitudinal range (ϕ) so that the longitudinal velocity components (V_ϕ) within a segment resemble a linear feature across the entire latitudinal range (θ) (Figure 2). Examination of the latitudinal velocity component (V_θ) shows that most segments are characterized by a near-zero velocity. Within each segment the velocity transition occurs at different latitudes (θ) and across various widths (Figure 2). It is noticeable that within segments 1-7 the normalized velocities do not reach zero, reflecting unsampled deformation east of the study area in the Basin and Range and the Eastern California Shear Zone [e.g., *Thatcher et al.,* 1999]. However, within segments 8-10, normalized velocities reach zero magnitude, reflecting a full transition in normalized velocity within the plate boundary zone spanned by the SCEC velocity field.

Using a best-fit smooth-spline algorithm, we model the variations of both velocity components in each segment, as a smooth undulating transition across the plate boundary (solid lines in Figure 2). The best-fit smooth spline uses a minimum χ^2 criteria to calculate a curve that best fits the data. The analysis relies on the assumptions that within each segment the velocity field is continuous and that the longitudinal velocity variations are negligible. Next, we calculate velocity gradients (dashed lines in Figure 2), which are the major components of the strain-rate tensor, by numerical differentiation. Figure 2 shows that the pattern and magnitude of the velocity gradients vary from one segment to the other and within each segment and that some of the segments are characterized by localized regions of high magnitude gradients. We also calculate velocity gradients by conducting the same analysis for 15 latitudinal profiles (Figure 1). In order to calculate longitudinal gradients we modified the assumption of negligible longitudinal velocity variations, allowing smooth velocity transitions along small distances across segment boundaries (tapering off the assumed velocity step function). This modification allows us to obtain more realistic gradient estimates, rather than assume infinite gradients at the boundaries.

The four velocity gradient components are used to calculate the regional distribution of strain rates in southern California and their invariant properties, the magnitude of shear strain rate (γ) and dilatation rate (Δ). The calculated gradients are assigned uniformly to the entire width of the segments and profiles and are summed in $0.01^\circ \times 0.01^\circ$ bins. Figure 3a shows that high magnitude right-lateral shear strain rate is localized along twelve belts with varying magnitudes (0.1-0.95 μstrain/year). The belts are located along segments of the SAFS (Figure 3b) and are of different lengths and widths. Unlike the localized shear deformation, dilatational deformation is diffuse and of relatively low magnitude (< 0.2 μstrain/year) (Figure 4a).

Discussion

Our analysis was conducted with no prior assumptions regarding the geology, tectonics, or seismicity of the region. Although preliminary knowledge of the location of active faults was used to choose geodetic survey sites, our analysis itself was free of these considerations. We were able to conduct such an analysis because we used a quasi two-dimensional deformation approach after choosing the most suitable PoD reference frame for the 349 SCEC velocity vectors. This approach is possible, because the velocity field follows predominantly the segmented fault arrangement of the SAFS. Thus, by dividing the velocity field into 10 segments of similar velocity and using one-dimensional mathematical operations, we were able to locate subtle and localized changes in the velocity field. The analysis produces regional shear strain rate and dilatation rate maps for southern California, which are compared below with geological and seismic observations.

Figure 3 shows that distribution of the shear deformation and its relation to the geographic location of major fault segments and microseismicity. The locations and lengths of the geodetically-determined shear belts coincide with the locations of major strike-slip fault segments of the SAFS (Figure 3b) and locally with regions of concentrated microseismicity

(Figure 3c). In Table 1, we list the velocity transition segments and their derived deformation parameters compared with geologic and seismic observations. Highest strain rate (0.95 μstrain/year) is observed along segment 1, which corresponds to the creeping Parkfield segment. Other well-defined belts with high strain rate (0.3-0.6 μstrain/year) are observed within the SAF-Cholame and SAF-Carrizo segments (segments 2 and 3) north of the big bend, and within the SAF-Coachella, Imperial and Cerro Prieto (northern Baja California) segments (segments 8b, 9 and 10) south of the big bend. We attribute the high strain rate in segments 9 and 10 to the narrow width of the plate boundary in this region and not to postseismic activity as suggested by *Jackson et al.* [1997]. Diffuse belts with lower magnitude shear strain rate (< 0.3 μstrain/year) are observed in segments 4, 5, 6b, and, 7b, corresponding to the SAF-Mojave segment, located along the big bend. Our analysis also detects three low magnitude parallel belts west of the big bend (segments 6a, 7a, and 8a), corresponding to secondary fault segments closer to the coast (San Jacinto Fault and Elsinore Fault-Glen Ivy segments) and within the highly populated Los Angeles basin (Newport-Inglewood segment). Although geologic and seismic observations indicate that segment 8 is characterized by three active parallel fault segments, our analysis failed to discern whether the westernmost Elsinore Fault is active because of the sparseness of the data west of this fault (Figure 1). Similarly the Agua Blanca Fault, which is located in Baja California (latitude 38.40° in Segment 10 of Figure 2), is not adequately sampled to determine whether or not it is active.

Figure 4 shows that distribution of the dilatational deformation and its relation to the geographic location of major fault segments and microseismicity. Unlike the localized shear deformation, dilatational deformation is diffuse and of relatively low magnitude (< 0.2 μstrain/year). The observed dilatation-rate pattern shows expansion along the southern part of the SAFS (blue in segments 8-10) and contraction in the northern part, west of the big bend (red in segments 4-6). This pattern agrees with the overall geological picture of extension along the Salton Trough and Imperial Valley and contraction along the big bend and westward. The highest contraction rate, detected in segments 5 and 6, reflects the ongoing contraction within the Ventura and Los Angeles basins. Our analysis also shows five pairs of low magnitude contraction-dilatation variations (Segments 3, 5, 8, 9, and 10), which are probably artifacts resulting from minor variations in the latitudinal velocity component (Figure 2).

Figure 3c and Figure 4c project the location of seismic activity during 1997, mostly microseismicity recently relocated by *Richards-Dinger and Shearer* [2000], onto the map of shear strain rate and dilatation rate, respectively. We chose to use the 1997 data set because it is a limited data set (13,908 out of 100,000 events) but is representative of the overall seismic pattern of the past 40 years in the region. These projections and Table 1 show that six of the high shear belts (segments 6a, 6b, 7b, 8a, 8b, and 9) are also characterized by a high level of microseismicity (> 150 events in 1997 - Table 1), as is the high contraction rate region in segment 5. The coincidence of the geodetically detected belts of high strain rates and high levels of microseismicity indicates that a significant part of the interseismic deformation occurs within the brittle upper crust (at depths of 4-10 km, Table 1), and not only below the seismogenic crust, as assumed by most models [e.g., *Savage et al.,* 1973]. Furthermore, the discontinuous distribution of the deformation field and high correlation with microseismicity indicates that the interseismic deformation along the SAFS is controlled by the strong brittle upper crust and not by a smooth, continuous flow in the weak lower crust, as has been recently suggested by *Bourne et al.* [1998].

Acknowledgments. This research was supported by the Southern California Earthquake Center. SCEC is funded by NSF Cooperative Agreement EAR-8920136 and USGS Cooperative Agreements 14-08-0001-A0899 and 1434-HQ-97AG01718. The SCEC contribution number for this paper is 573. We thank SCEC's Crustal Deformation Working Group for use of the SCEC velocity model version 2.0, D. Steinberg for his help in formulating the statistics for the calculations, and L. Prawirodirdjo for her help in preparation of the manuscript. We are thankful to Bill Holt and an anonymous reviewer for their helpful comments.

References

Bennett, R. A., W. Rodi, and R. E. Reilinger, Global Positioning System constraints on fault slip rates in southern California and northern Baja, Mexico, *J. Geophys. Res., 101,* 21,943-21,960, 1996.

Bourne, S. J., P. C. England, and B. Parsons, The motion of crustal blocks driven by flow of the lower lithosphere and implications for slip rates of continental strike-slip faults, *Nature, 391,* 655-659, 1998.

DeMets, C. and T. Dixon, New kinematic models for Pacific-North America motion from 3 MA to present, I: Evidence for steady motion and biases in the NUVEL-1A model, *Geophys. Res. Lett., 26,* 1921-1924, 1999.

Grant, L. B., J. T. Waggoner, T. Rockwell, and C. vonStein, Paleoseismicity of the north branch of the Newport-Inglewood fault zone in Huntington Beach, California, from cone penetrometer test data, *Bull. Seismol. Soc. Am., 87,* 277-293, 1997.

Humphreys, E. D., and R. J. Weldon II, Deformation across the western United States: A local estimate of Pacific-North America transform deformation, *J. Geophys. Res., 99,* 19,975-20,010, 1994.

Jackson, D. D., Z.-K. Shen, D. Potter, X.-B. Ge, and L. Sung, Southern California deformation, *Science, 277,* 1621-1622, 1997.

Richards-Dinger, K. B., and P. M. Shearer, Earthquake locations in southern California obtained using source specific station terms, *J. Geophys. Res.,* 10,939-10,960, 2000.

Savage, J. C. and J. Burford, Geodetic determination of relative plate motion in central California, *J. Geophys. Res., 78,* 832-845, 1973.

Shen-Tu, B., W. E. Holt, and A. J. Haines, Deformation kinematics in the western United States determined from Quaternary fault slip rates and recent geodetic data, *J. Geophys. Res., 104,* 28,927-28,955, 1999.

Thatcher, W., G. R. Foulger, B. R. Julian, J. Svarc, E. Quilty, and G. W. Bawden, Present-day deformation across the Basin and Range province, Western United States, *Science, 283,* 1714-1718, 1999.

Wdowinski, S., A theory of intraplate tectonics, *J. Geophys. Res., 103,* 5037-5059, 1998.

Working Group on California Earthquake Probabilities, Seismic hazard in Southern California: probable earthquakes, 1994 to 2024, *Bull. Seismol. Soc. Am., 85,* 379, 1995.

Shimon Wdowinski and Yonadav Sudman, Department of Geophysics and Planetary Sciences, Tel Aviv University Ramat Aviv, Israel.

Yehuda Bock, IGPP, Scripps Institution of Oceanography, La Jolla, California.

(Received November 14, 2000; revised February 28, 2001; accepted March 6, 2001.)